ACTA IMEKO
ISSN: 2221-870X
December 2026, Volume 15, Number 4, 1 – 8

Full-field characterization of strain localization and damage evolution in additively manufactured continuous carbon fiber-reinforced polyamide 6 under compression

Andrija Zaplatić[1], Lovorka Maršić[1], Ivica Smojver[1], Fran Ušurić[1], Zvonimir Tomičević[1]

[1] *Faculty of Mechanical Engineering and Naval Architecture, University of Zagreb, 10 000 Zagreb, Croatia*

ABSTRACT
This paper investigates the compressive behavior of additively manufactured polyamide 6 composites reinforced with continuous carbon fibers and loaded along the fiber direction. Unidirectionally reinforced specimens were manufactured by continuous fiber co-extrusion and subjected to monotonic and cyclic compression in accordance with ASTM D695. Prior to mechanical testing, X-ray computed tomography was used to assess manufacturing-induced porosity, while digital image correlation provided full-field kinematic measurements throughout loading.
Both specimens reached an ultimate compressive stress of approximately 99 MPa, with measured porosity levels ranging from 11 to 14 %. Under monotonic loading, strain progressively localized with increasing load, while post-failure observations revealed local crushing, fiber kinking, longitudinal splitting, and interlaminar delamination. Cyclic loading resulted in pronounced hysteresis, accumulation of irreversible strain, and progressive stiffness degradation. The digital image correlation fields captured the evolution and localization of longitudinal and transverse strains, while the correlation residuals provided complementary information on local surface changes associated with damage. The results demonstrate the capability of full-field digital image correlation measurements to characterize strain localization and damage evolution in additively manufactured continuous carbon fiber-reinforced polyamide 6 composites under compressive loading.

Section: RESEARCH PAPER

Keywords: additive manufacturing; continuous carbon fiber-reinforced composites; compression testing; digital image correlation; X-ray computed tomography; damage evolution

Citation: A. Zaplatić, L. Maršić, I. Smojver, F. Ušurić, Z. Tomičević, Full-field characterization of strain localization and damage evolution in additively manufactured continuous carbon fiber-reinforced polyamide 6 under compression, Acta IMEKO, vol. 15 (2026) no. 4, pp. 1–8. DOI: 10.21014/actaimeko.v15i4.2493

Section Editor: Emina Hadzalic, University of Rijeka, Croatia

Received: August 18, 2026; **In Final Form:** September 29, 2026; **Published:** December 2026.

Copyright: This is an open-access article distributed under the terms of the Creative Commons Attribution 4.0 International License.

Funding: This work has been funded by the European Union (NextGenerationEU) under the National Recovery and Resilience Plan 2021–2026 (NRRP), through the UNIZAG FSB institutional project "Generative design based on experimental and numerical modelling - GENEXPERT", approved by the Ministry of Science, Education and Youth of the Republic of Croatia (component C3.2, source 581), and the Croatian Science Foundation project IP-2022-10-8845 DENNGA.

Corresponding Author: Zvonimir Tomičević, e-mail: zvonimir.tomicevic@fsb.unizg.hr

1. INTRODUCTION

Composite materials have become an important class of engineering materials owing to their high stiffness, high strength-to-mass ratio, low density, and the possibility of tailoring their properties to specific requirements. These characteristics have led to their widespread use in aerospace, marine, automotive, biomedical, and other sectors where weight reduction and durability are essential [1], [2]. In aerospace applications, for example, composite materials are extensively used in structural components, such as wings and fuselage sections. Interest in advanced composite materials and their manufacturing technologies has continued to increase due to the demand for lighter and more efficient structures [3], [4].

Additive manufacturing has emerged as an alternative to conventional manufacturing technologies, enabling the fabrication of complex geometries while reducing manufacturing time and post-processing requirements [5]. Although fused deposition modeling is widely used for polymeric materials, unreinforced thermoplastics generally exhibit limited interlayer bonding and relatively low mechanical properties, restricting their use in load-bearing structural applications [6], [7]. To overcome these limitations, advanced extrusion-based processes have been developed, in which continuous reinforcing fibers are embedded within the polymer matrix during printing [8]. The incorporation of continuous fibers can substantially improve the mechanical performance of additively manufactured components [8], [9]. Carbon fibers are particularly attractive as reinforcement because of their high specific stiffness and strength [4].

Digital image correlation (DIC) is a versatile non-contact op-

tical measurement technique for full-field kinematic analysis [10]–[13]. Its applicability spans a wide range of length scales, from microscopic [14] to macroscopic applications [15]. Two principal DIC formulations are commonly distinguished: local [16] and global [17]. In the global DIC approach, the region of interest (ROI) is discretized using a finite element (FE) mesh, with displacement continuity enforced through the FE shape functions [18]. DIC has been successfully applied to characterize material behavior under a wide range of loading conditions, including tensile [19], compressive [20], and multiaxial loading [21]. The availability of full-field kinematic measurements is particularly relevant for heterogeneous materials, for which strain localization and damage may not be adequately described by global measurements alone.

In additively manufactured continuous fiber-reinforced composites, the compressive response can be strongly influenced by the heterogeneous internal architecture and by localized deformation mechanisms. Consequently, combining information on the internal structure with full-field measurements of surface kinematics provides a suitable framework for investigating the onset and evolution of damage under compression. In particular, X-ray computed tomography (XCT) enables the quantification of manufacturing-induced porosity, while DIC provides full-field measurements of the evolving surface kinematics throughout mechanical loading.

The present study investigates the compressive behavior and damage evolution of additively manufactured continuous carbon fiber-reinforced polyamide 6 composites subjected to monotonic and cyclic loading along the fiber direction. XCT is employed to quantify manufacturing-induced porosity [22], while global DIC provides full-field measurements of surface kinematics [23] throughout loading. Particular attention is devoted to the evolution and localization of longitudinal and transverse strain fields and their relationship with the correlation residuals. For cyclic loading, stiffness degradation is additionally quantified using a damage variable derived from the evolution of the effective Young's modulus. The combined measurements provide insight into strain localization and the progressive damage mechanisms governing the compressive response of additively manufactured continuous carbon fiber-reinforced PA6 composites.

The novelty of this study lies in the complementary application of XCT and DIC to investigate the deformation and damage behaviour of continuous carbon fiber composites under compressive loading. Previous studies have employed XCT to characterize the internal architecture of composite materials and quantify manufacturing-induced features, such as porosity [24], [25]. The combined use of XCT and DIC for this purpose remains relatively scarce in the existing literature. However, characterization of the internal structure alone does not provide information on how deformation localizes and evolves during mechanical loading. In the present study, XCT is performed prior to mechanical testing to characterize the initial internal architecture and determine the porosity volume fraction, while DIC is used during compression to obtain full-field measurements of the surface deformation. The complementary application of the two techniques provides information on both the initial internal state of the material and the evolution and localization of deformation during loading, thereby contributing to the identification of the mechanisms associated with damage development under compression.

2. MATERIAL AND METHODOLOGY

The investigated material was a continuous fiber-reinforced polymer matrix composite manufactured using the composite fiber co-extrusion process. The matrix consisted of polyamide 6, reinforced with continuous carbon fiber tows with a diameter of 0.28 mm. The fiber tows comprise individual carbon fibers pre-impregnated with PA6 to facilitate bonding with the surrounding matrix during extrusion. Both specimens were manufactured with the same unidirectional reinforcement architecture using an Anisoprint Composer A3 printer. During printing, the thermoplastic matrix filament was extruded through a heated nozzle, while the continuous fiber tows were co-extruded along the prescribed deposition paths.

The carbon fiber-reinforced specimens were prepared in accordance with ASTM D695 [26]. To ensure consistent manufacturing conditions, a rectangular composite beam with dimensions of $95 \times 14 \times 14$ mm^3 was initially printed. The test specimens were subsequently extracted from the beam by waterjet cutting to obtain the final dimensions of $28 \times 14 \times 14$ mm^3.

Prior to mechanical testing, the specimens were examined using XCT to characterize their internal architecture and manufacturing-induced defects. Scanning parameters are listed in Table 1. Particular attention was devoted to the spatial distribution and volume fraction of porosity. The volume fraction of porosity was determined by sample volume segmentation to extract the pore volume. The segmentation was performed using Fiji software [27], where the gray levels corresponding to the voids were chosen using the Otsu segmentation method [28]. The CT volume was converted into a binary image by applying an intensity threshold to distinguish the voids from the fiber/matrix material. Next, the void volume fraction was calculated as the ratio of the segmented void volume to the total volume of the CT scan. Figure 1 shows representative mid-section slices perpendicular to the longitudinal direction of the fiber tows for the specimens subsequently subjected to monotonic and cyclic compression. The porosity volume fractions, quantified over the entire reconstructed volumes, are 11 % for the former and 14 % for the latter.

Two compression tests were performed. The experimental campaign consisted of an initial monotonic (M) quasi-static compression test with continuously increasing load, followed by a cyclic (C) compression test on a separate specimen. The monotonic compression was applied to the sample until post-peak stress reduction, i.e. softening, occurred.

Table 1. Hardware parameters of the CT scans

CT scanner	WENZEL® exaCT® S130
X-Ray source	Hamamatsu L9181-02
Filter	Filter for polymers
Voltage	130 kV
Current	64 μA
Integration time	2.5 s
Detector - X-ray source distance	205 mm
Object - X-ray source distance	72 mm
Detector	Flat detector (3Mpx)
Detector definition	2304 × 1300 px
Voxel size	15.6 μm
Reconstruction	Feldkamp-Davis-Kress method
Scanning settings	High quality
Number of projections	720
Angular amplitude	360°
Frame averaging	None
Acquisition duration	2 h 9 min 18 s
Gray level amplitude	16 bit converted to 8 bit
Field of view	15.97 × 30.47 × 13.74 mm³

After reaching the maximum load of 18.5 kN, the load decreased, and the test was terminated when it reached 5 kN, due to the loss of load-carrying capacity and excessive out-of-plane displacements. The loading levels applied during the cyclic test

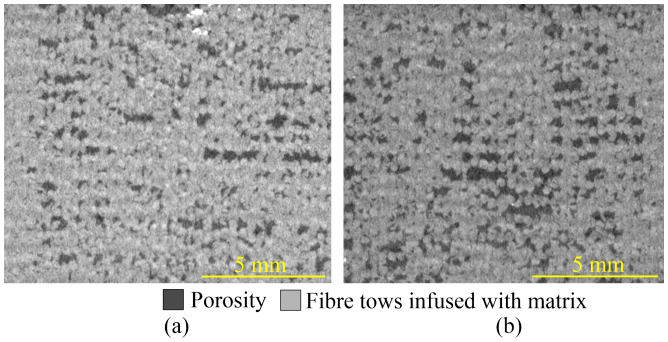


Figure 1. CT mid-section slices perpendicular to the fiber tow orientation for specimens subjected to (a) monotonic (M) and (b) cyclic (C) compressive loading.

were defined based on the response obtained from the monotonic experiment, and a total of 10 loading–unloading cycles were performed.

In both tests, compression was applied parallel to the direction of the continuous fibers. The experiments were carried out using a Messphysik Beta 50-5 uniaxial testing machine (Figure 2, label 4) under displacement control at a crosshead rate of 1.3 mm/min. For the cyclic experiment, the displacement amplitude progressively increased by 0.2 mm per cycle until the compression of 2 mm was reached. Furthermore, the loading rate was consistent for both loading and unloading phases of the experiment without any dwell periods, i.e. the loading/unloading was continuous. During each loading cycle, the specimen was unloaded until the applied load reached the initial preload of 500 N, after which loading was resumed.

Full-field surface kinematics were measured using DIC throughout the experiments [29]. A global DIC formulation was employed, in which the image ROI was discretized using a FE mesh. The displacement field $\mathbf{u}(\mathbf{x})$ was determined by minimizing the gray-level differences between the reference and deformed images. The image-matching contribution to the correlation functional is written as

$$\Phi^2 = \sum_{\mathrm{ROI}} \left\| f(\mathbf{x}) - g\left(\mathbf{x} + \mathbf{u}(\mathbf{x})\right) \right\|^2, \tag{1}$$

where $f(\mathbf{x})$ denotes the reference image, and $g(\mathbf{x} + \mathbf{u}(\mathbf{x}))$ represents the deformed image corrected by the trial displacement field. In the employed global DIC analysis, the image-matching criterion was combined with regularization to improve the robustness of the measured displacement fields. The corresponding correlation parameters are reported in Table 2.

The optical setup consisted of a single digital camera equipped with a telecentric lens (Figure 2, labels 2 and 3, respectively). Two LED panels (label 1) provided uniform illumination of the specimen surface, while a black matte curtain (label 5) was used to shield the measurement area from ambient light and minimize

Table 2. Software parameters of the DIC analyses

DIC software	Correli 3.0
Element size	32 px
Shape functions	Linear
Mesh	T3
Matching criterion	Penalized sum of square differences
Regularization	256 px
Interpolation	Linear

variations in illumination during testing. The main optical hardware parameters are listed in Table 3, while the parameters used for the DIC analyses are provided in Table 2. Mechanical regularization [30], [31] was used in the correlation procedure, which acts as a low-pass filter on the displacement field. A regularization

Table 3. Hardware parameters of the 2D optical setup

Setup	2D setup
Camera	Manta G145B ASG
Definition	1388 × 1038 px
Gray levels rendering	8 bit
Lens	0.25 × – 0.5 × VariMagTL™
Magnification	0.25 ×
Distance ring	-
Aperture	22
Field of view	35.8 × 26.67 mm²
Image scale	0.0258 mm/px
Stand off distance	145 mm
Patterning technique	B/W speckle pattern
Lighting	Dual LED panels

length of 256 pixels (6.6 mm in physical space, i.e., slightly less than half the specimen width) was used. This parameter defines the characteristic spatial scale over which regularization acts on the displacement field, and thereby controls the spatial smoothness of the resulting displacement solution. The selected value was used to suppress displacement fluctuations associated with measurement uncertainty while preserving the characteristic spatial features of the displacement field.

3. RESULTS

The results obtained from the monotonic and cyclic compression tests are presented in this section. First, the evolution of the average longitudinal, transverse, and shear strain components obtained from DIC is analyzed. The average strains were calculated over a virtual gauge located in the central region of each specimen by averaging the corresponding nodal strain values. Selected loading stages are subsequently

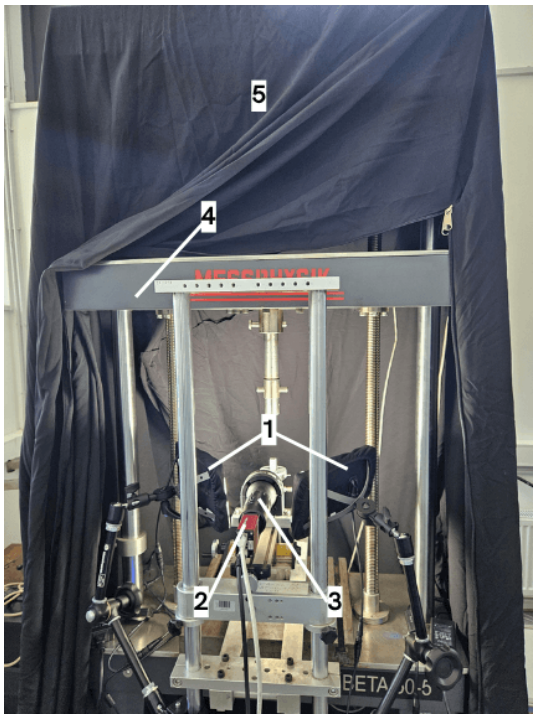


Figure 2. Labels: (1) LED panels, (2) digital camera, (3) telecentric lens, (4) uniaxial testing machine, and (5) black matte curtain.

examined using the full-field longitudinal and transverse strain distributions and the corresponding correlation residuals. Furthermore, correlation residuals are displayed for the selected stages. The residuals display areas where the algorithm could not account for severe changes in the gray levels between the reference and the

corrected deformed image. It should be noted that the increased residuals are not caused only by surface damage, but can also be caused by out-of-plane motions, changes in illumination or image contrast, and degradation of the speckle pattern. Therefore, the correlation residuals are not interpreted as a direct measurement of physical damage. In the present study, regions of increased residuals are interpreted in conjunction with the observed strain localization and post-failure surface observations to support the identification of damage-related surface changes.

3.1. Monotonic compression (M)

The evolution of the average strain components for the specimen subjected to monotonic compression is presented in Figure 3. The longitudinal strain ε_x, corresponding to the loading direction, exhibits the largest magnitude throughout most of the experiment. The transverse strain ε_y progressively increases with loading, while the shear strain ε_{xy} remains comparatively small. Four characteristic loading stages were selected for further full-field analysis, corresponding to stress levels of 28 MPa, 72 MPa, the ultimate compressive stress (UCS) of 99 MPa, and a post-peak stress of 80 MPa. Out-of-plane deformation became apparent after the UCS was reached and progressively intensified during the post-peak softening regime, eventually limiting the applicability of the 2D DIC measurements.

The evolution of the longitudinal strain field during monotonic compression is shown in Figure 4. At the first loading stage (Figure 4(a)), the longitudinal strain magnitude is low and the field remains relatively uniform over the observed surface. With increasing load (Figure 4(b)), the strain magnitude increases, while no pronounced localization is observed across the specimen. At the UCS (Figure 4(c)), a localized strain region develops near the right edge of the specimen. This localization becomes more pronounced during post-peak softening (Figure 4(d)).

The corresponding transverse strain fields are presented in Figure 5. At the first loading stage (Figure 5(a)), the transverse strain field is relatively uniform, similarly to the longitudinal strain field. At 72 MPa (Figure 5(b)), a localized strain concentration develops in the central region of the ROI. At the UCS (Figure 5(c)), the magnitude and spatial extent of this localization increase. During post-peak softening (Figure 5(d)), the localized region extends towards the right specimen edge as denoted by the green ellipse, indicating increasingly heterogeneous deformation.

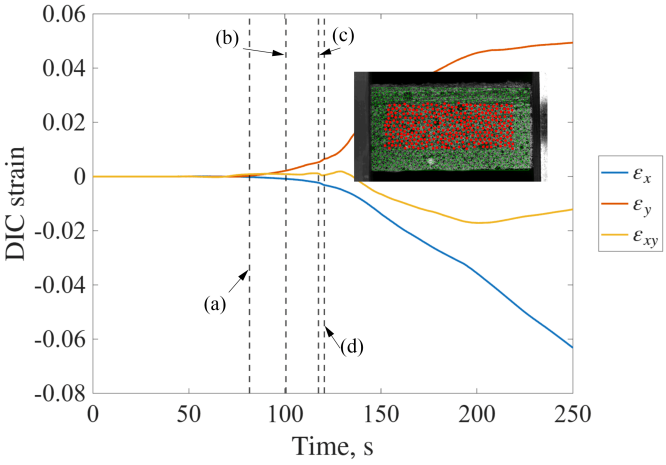


Figure 3. Evolution of the average DIC strain components during the monotonic compression test (M). The four loading stages analyzed in the following sections are marked: (a) 28 MPa, (b) 72 MPa, (c) 99 MPa, and (d) 80 MPa. The inset shows the virtual strain gauge and the highlighted nodes used to compute the average strain.

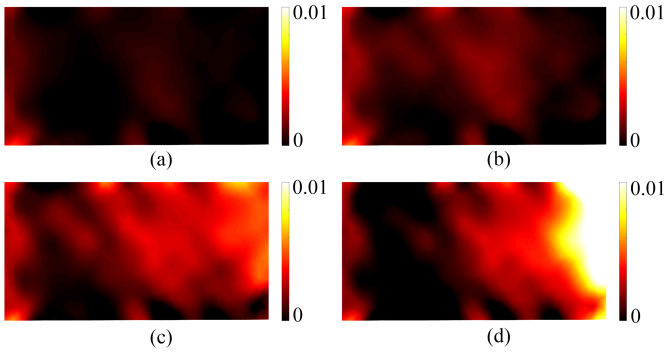


Figure 4. Longitudinal strain fields ε_x measured by DIC during the monotonic compression test (M) at (a) 28 MPa, (b) 72 MPa, (c) 99 MPa, and (d) 80 MPa.

The correlation residual maps shown in Figure 6 provide complementary information on local changes in the specimen surface that cannot be represented by the measured displacement field. At the first loading stage (Figure 6(a)), the residuals remain relatively uniform over most of the ROI. The increased residuals observed near the left edge are associated with the vicinity of the specimen–platen contact. At 72 MPa (Figure 6(b)), increased residuals appear in the central region of the ROI and spatially coincide with the transverse strain localization. At the UCS and during the subsequent post-peak stage (Figure 6(c) and (d), respectively), the highest residuals are concentrated near the right edge of the ROI highlighted with green ellipses. This region also coincides with the pronounced localization observed in both the longitudinal and transverse strain fields, indicating progressive surface changes associated with damage development. The regions denoted by the green ellipses in the transverse strain and residual fields correspond to the location where fiber splitting was subsequently observed.

3.2. Cyclic compression (C)

Specimen C was subjected to 10 loading–unloading cycles with progressively increasing maximum imposed displacement. As in the monotonic experiment, the longitudinal and transverse strains represent the dominant strain components, whereas the shear strain remains comparatively small during the initial cycles and increases after the UCS is reached (Figure 7). Four characteristic loading stages were selected for further analysis: the peak stress of an early loading cycle (i.e., elastic regime) at 30 MPa, the peak stress of a cycle preceding the UCS at 78 MPa, the UCS of 99 MPa, and the peak stress of the first subsequent cycle at 71 MPa. Beyond this stage, out-of-plane deformation became too pronounced for reliable analysis using 2D DIC.

The longitudinal strain fields for the selected loading stages are presented in Figure 8. At the first selected stage (Figure 8(a)),

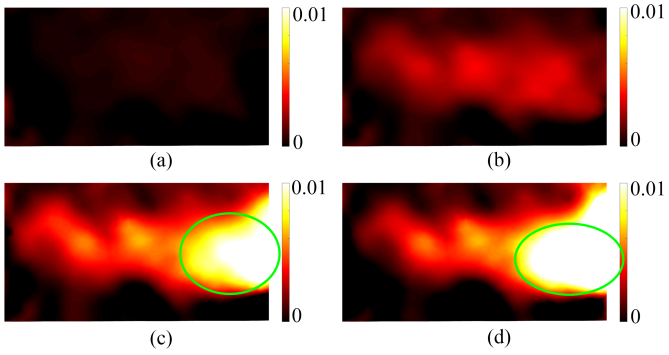


Figure 5. Transverse strain fields ε_y measured by DIC during the monotonic compression test (M) at (a) 28 MPa, (b) 72 MPa, (c) 99 MPa, and (d) 80 MPa.

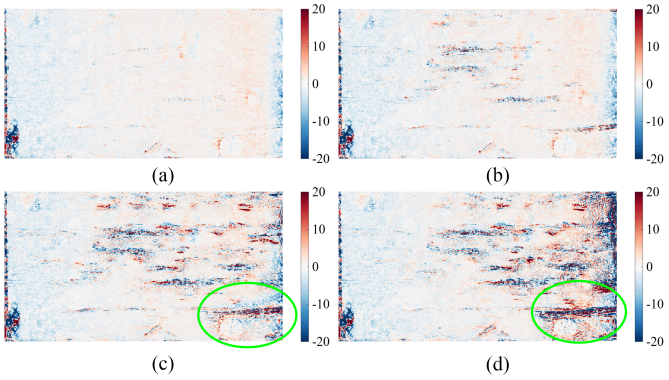


Figure 6. Correlation residuals for the monotonic compression test (M) at (a) 28 MPa, (b) 72 MPa, (c) 99 MPa, and (d) 80 MPa expressed in gray levels. The green ellipses highlight regions associated with subsequently observed fiber splitting.

a weak strain localization is observed in the central region of the ROI. However, the corresponding correlation residual map (Figure 10(a)) does not exhibit a distinct feature in this region. At 78 MPa (Figure 8(b)), the strain magnitude is approximately one order of magnitude higher, while a similar localization pattern persists, indicating that the observed strain localization is associated with the applied compressive loading. At the UCS (Figure 8(c)) and during the subsequent cycle (Figure 8(d)), the dominant strain localization shifts towards the right edge of the specimen, resulting in an increasingly heterogeneous strain field.

The transverse strain fields are shown in Figure 9. At the first selected loading stage (Figure 9(a)), a localized region is already visible near the right side of the specimen (denoted by a purple ellipse). A corresponding feature is observed in the correlation residual map (Figure 10(a)), suggesting that the transverse strain localization is associated with local changes in the specimen surface. At the subsequent loading stages (Figure 9(b)–(d)), the same localization pattern persists while its magnitude progressively increases. In contrast, the remainder of the observed surface remains comparatively homogeneous.

The correlation residual fields presented in Figure 10 reveal a pronounced residual band near the right side of the specimen, spatially coinciding with the localization observed in the transverse strain fields (denoted with purple ellipses). This feature is already visible at the first selected loading stage (Figure 10(a)). At higher loading levels (Figure 10(b)–(d)), the residual band becomes increasingly pronounced and is accompanied by additional

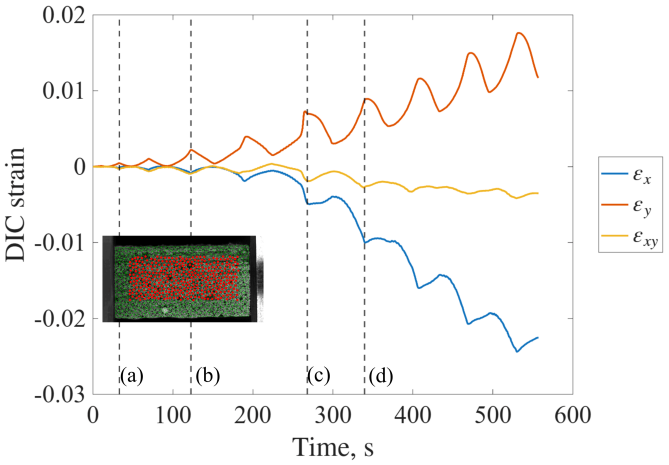


Figure 7. Evolution of the average DIC strain components during the cyclic compression test (C). The four loading stages analyzed in the following sections are marked: (a) 30 MPa, (b) 78 MPa, (c) 99 MPa, and (d) 71 MPa. The inset shows the virtual strain gauge and the highlighted nodes used to compute the average strain.

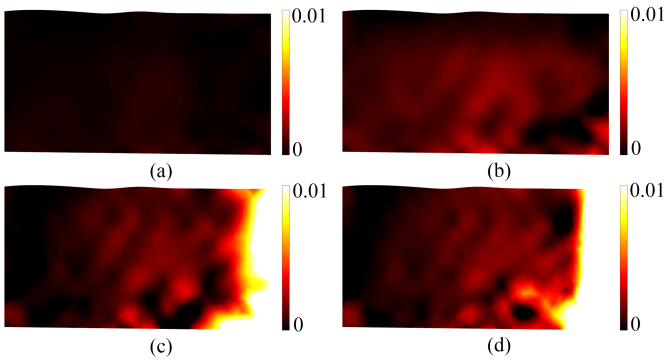


Figure 8. Longitudinal strain fields ε_x measured by DIC during the cyclic compression test (C) at (a) 30 MPa, (b) 78 MPa, (c) 99 MPa, and (d) 71 MPa.

longitudinal residual concentrations. These regions indicate local changes in gray levels that cannot be compensated by the measured displacement field, and are consistent with progressive surface damage during cyclic loading. Furthermore, the location and geometry of these features are consistent with the fiber splitting subsequently observed after the test.

4. DISCUSSION

The monotonic and cyclic compression responses are compared in Figure 11. The effective Young's modulus was determined from the linear portion of the stress–strain response, yielding approximately 30 GPa for specimen M and an initial value of approximately 33 GPa for specimen C. The stress–strain responses, based on the average longitudinal strains obtained by DIC, show that both specimens reached the UCS of approximately 99 MPa

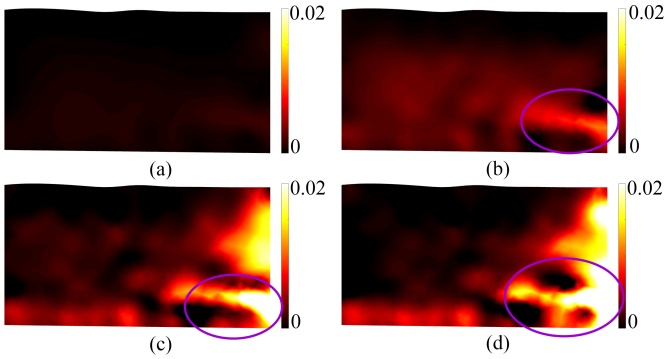


Figure 9. Transverse strain fields ε_y measured by DIC during the cyclic compression test (C) at (a) 30 MPa, (b) 78 MPa, (c) 99 MPa, and (d) 71 MPa. The strain localization is denoted by purple ellipses.

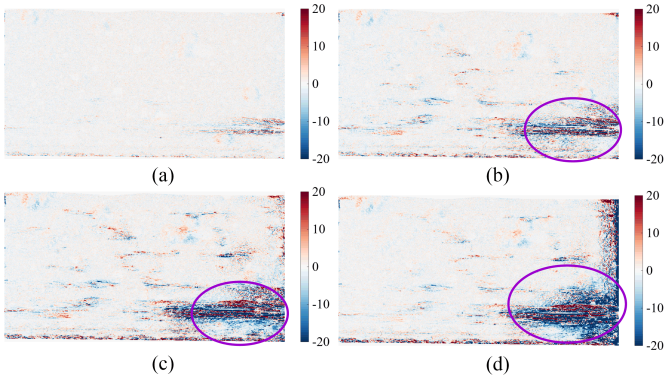


Figure 10. Correlation residuals for the cyclic compression test (C) at (a) 30 MPa, (b) 78 MPa, (c) 99 MPa, and (d) 71 MPa expressed in gray levels. The purple ellipses highlight regions associated with subsequently observed fiber splitting.

at comparable average strain levels. Prior to the UCS, neither specimen exhibited pronounced global bending. Instead, the DIC fields revealed a progressive transition from relatively homogeneous deformation to localized longitudinal and transverse strain concentrations. Although specimen C exhibited a higher porosity volume fraction than specimen M, both specimens reached approximately the same UCS. However, given that only one specimen was tested for each loading protocol, no general conclusion regarding the influence of porosity on the compressive strength can be drawn. Following the UCS, specimen C maintained higher stress levels than specimen M during the post-peak response; however, this difference should be interpreted in the context of the different loading histories of the two specimens.

The post-failure configurations of the two specimens are presented in Figure 12. Following monotonic compression, specimen M exhibits pronounced lateral deformation accompanied by local crushing in the highly compressed region (Figure 12(a) and (b)). The side views further reveal fiber kinking (purple ellipses), longitudinal splitting, interlaminar delamination (green rectangles), and separation between adjacent deposited fiber paths. These observations indicate that failure resulted from a combination of local compressive instability, fiber kinking, fiber-path separation, and interlaminar delamination rather than from a single dominant failure mechanism.

Following cyclic compression, specimen C exhibits local fiber kinking, out-of-plane buckling, and extensive interlaminar delamination (Figure 12(c) and (d)). Pronounced separation along the deposited fiber paths is accompanied by localized buckling and fiber kinking. The locations of these post-failure features are consistent with the regions of pronounced strain localization and increased correlation residuals identified by DIC during loading. This agreement indicates that the full-field measurements captured the progressive development of strain localization preceding final failure.

To quantify the progressive stiffness degradation during cyclic loading, a stiffness-based damage variable was calculated as

$$D = 1 - \frac{E}{E_0}, \tag{2}$$

where E is the effective Young's modulus determined for each loading cycle and E_0 is the initial Young's modulus obtained from the first cycle.

The effective Young's modulus E was determined by fitting a straight line to the linear-elastic region of the stress–strain curve and calculating its slope. Linear least-squares regression was applied exclusively to data extracted from the loading branches. To ensure a consistent comparison of the effective stiffness between cycles, the stress interval used for fitting was kept constant at 16–42 MPa for cycles 2–10. This interval was selected to exclude the initial nonlinear response. Since the first loading cycle reached a lower maximum stress, a stress interval of 6–15 MPa was used for this cycle. The stress and corresponding strain ranges used for each cycle are listed in Table 4. The evolution of the damage variable, calculated from the effective modulus derived from the DIC-based stress–strain response, is shown in Figure 13. By the second loading cycle, D increases to approximately 0.16, indicating a marked reduction in effective stiffness at an early stage of cyclic loading. The damage variable subsequently increases to approximately 0.84 by the fifth cycle, and remains nearly unchanged during the sixth cycle. It then increases rapidly to approximately 0.95, before gradually approaching a plateau close to $D = 1$ during the final loading cycles. This evolution reflects the progressive degradation of the effective stiffness associated with increasing levels of irreversible strain and progressive damage during cyclic compression.

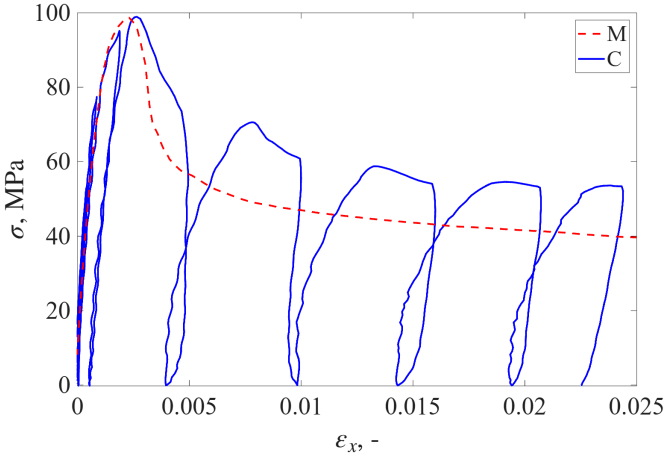


Figure 11. Comparison of the stress–longitudinal strain responses of the monotonic (M) and cyclic (C) compression tests.

5. CONCLUSIONS

The compressive behavior of additively manufactured PA6 composites reinforced with continuous carbon fibers was investigated under monotonic and cyclic loading parallel to the fiber direction. Both specimens reached an UCS of approximately 99 MPa, with measured porosity volume fractions ranging from 11 to 14 %. Although the two specimens exhibited different porosity levels, the limited number of tested specimens does not allow a general conclusion to be drawn regarding the influence of porosity on the compressive response.

Under monotonic loading, the DIC measurements revealed a progressive transition from relatively homogeneous deformation to pronounced longitudinal and transverse strain localization as the UCS was approached. Post-failure observations showed local crushing, fiber kinking, longitudinal splitting, separation between deposited fiber paths, and interlaminar delamination. Under cyclic loading, pronounced hysteresis and accumulation of irreversible strain were accompanied by progressive stiffness degradation. The DIC strain fields captured the evolution of strain localization, while the correlation residuals provided complementary information that, together with strain localization and post-failure observations, supported the interpretation of progressive surface damage. Consistently, the stiffness-based damage variable increased with the number of loading cycles, reflecting the progressive reduction in the effective Young's modulus.

The results demonstrate the capability of full-field DIC measurements to characterize strain localization and stiffness degradation in additively manufactured continuous carbon fiber-reinforced PA6 composites under compression. Future work

Table 4. Stress and strain intervals used for the determination of the effective Young's modulus for each loading cycle.

Cycle	σ, MPa	ε_x, %
1	6-15	0-0.03
2	16-42	0.01-0.11
3	16-42	0.04-0.26
4	16-42	0.09-0.39
5	16-42	0.26-0.76
6	16-42	0.63-1.21
7	16-42	4.9-6.6
8	16-42	10.7-12.5
9	16-42	15.6-17.7
10	16-42	20.5-22.1

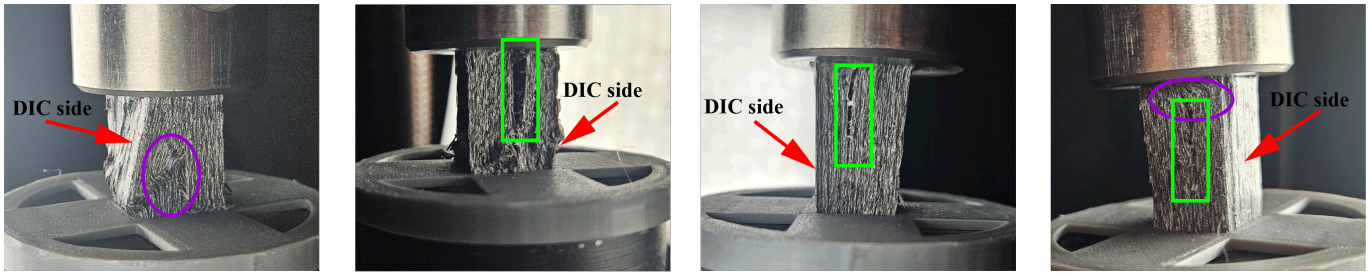


Figure 12. Post-failure configurations of the continuous carbon fiber-reinforced composite specimens subjected to (a,b) monotonic compression (M) and (c,d) cyclic compression (C). The right- and left-side views are shown for each specimen. Purple ellipses indicate localized fiber kinking, whereas green rectangles highlight interlaminar delamination.

should include a larger number of specimens to assess the repeatability and statistical significance of the observed behavior, as well as stereo DIC [32] to account for the pronounced out-of-plane deformation observed at advanced stages of loading.

AUTHORS' CONTRIBUTION

Andrija Zaplatić: Conceptualization, Data curation, Formal analysis, Investigation, Methodology, Supervision, Visualization, Writing - original draft

Lovorka Maršić: Conceptualization, Data curation, Formal analysis, Investigation, Methodology

Ivica Smojver: Investigation, Resources

Fran Ušurić: Investigation, Resources

Zvonimir Tomičević: Conceptualization, Data curation, Formal analysis, Investigation, Methodology, Supervision, Visualization

6. ACKNOWLEDGMENT

This work has been funded by the European Union (NextGenerationEU) under the National Recovery and Resilience Plan 2021–2026 (NRRP), through the UNIZAG FSB institutional project "Generative design based on experimental and numerical modelling - GENEXPERT", approved by the Ministry of Science, Education and Youth of the Republic of Croatia (component C3.2, source 581), and the Croatian Science Foundation project IP-2022-10-8845 DENNGA.

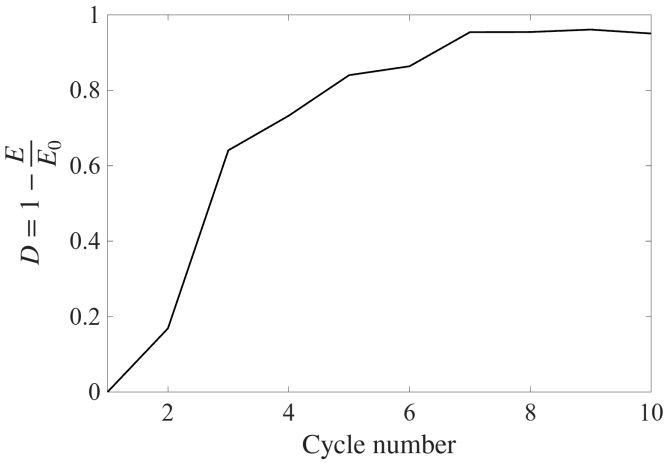


Figure 13. Evolution of the stiffness-based damage variable D as a function of the loading cycle for specimen C.

REFERENCES

[1] M. E. Torbali, A. Zolotas, N. P. Avdelidis, A state-of-the-art review of non-destructive testing image fusion and critical insights on the inspection of aerospace composites towards sustainable maintenance repair operations, Applied Sciences, vol. 13, 2023, p. 2732.
DOI: 10.3390/app13042732

[2] F. Khan, N. Hossain, J. J. Mim, S. M. Rahman, M. J. Iqbal, M. Billah, M. A. Chowdhury, Advances of composite materials in automobile applications – a review, Journal of Engineering Research, 2024.
DOI: 10.1016/j.jer.2024.02.017

[3] G. A. Pacheco, The Essentials of Composite Materials: A Guide for Engineering and Beyond, 1st ed., CRC Press, Boca Raton, FL, 2026, ISBN: 978-1-032-93279-8.
DOI: 10.1201/9781003565222

[4] I. M. Daniel, O. Ishai, Engineering Mechanics of Composite Materials, 2nd ed., Oxford University Press, New York, 2006, ISBN: 978-0195150971.

[5] M. A. Jamal, O. R. Shah, U. Ghafoor, Y. Qureshi, M. R. Bhutta, Additive manufacturing of continuous fiber-reinforced polymer composites via fused deposition modelling: A comprehensive review, Polymers, vol. 16, 2024, no. 12, p. 1622.
DOI: 10.3390/polym16121622

[6] S. Valvez, P. Santos, J. M. Parente, M. P. Silva, P. N. B. Reis, 3D printed continuous carbon fiber reinforced PLA composites: A short review, Procedia Structural Integrity, vol. 25, 2020, pp. 394–399.
DOI: 10.1016/j.prostr.2020.04.056

[7] J. M. Chacón, M. A. Caminero, P. J. Núñez, E. García-Plaza, I. García-Moreno, J. M. Reverte, Additive manufacturing of continuous fibre reinforced thermoplastic composites using fused deposition modelling: Effect of process parameters on mechanical properties, Composites Science and Technology, vol. 181, 2019, p. 107688.
DOI: 10.1016/j.compscitech.2019.107688

[8] F. Lupone, E. Padovano, C. Venezia, C. Badini, Experimental characterization and modeling of 3D printed continuous carbon fibers composites with different fiber orientation produced by FFF process, Polymers, vol. 14, 2022, no. 3, p. 426.
DOI: 10.3390/polym14030426

[9] M. Araya-Calvo, I. López-Gómez, N. Chamberlain-Simon, J. L. León-Salazar, T. Guillén-Girón, J. S. Corrales-Cordero, O. Sánchez-Brenes, Evaluation of compressive and flexural properties of continuous fiber fabrication additive manufacturing technology, Additive Manufacturing, vol. 22, 2018, pp. 157–164.
DOI: 10.1016/j.addma.2018.05.007

[10] A. Vrgoč, Z. Tomičević, A. Zaplatić, F. Hild, Damage analysis in glass fibre reinforced epoxy resin via digital image correlation, Transactions of FAMENA, vol. 45, 2021, no. 2, pp. 1–12.
DOI: 10.21278/TOF.452024020

[11] J. Holmes, S. Sommacal, R. Das, Z. Stachurski, P. Compston, Digital image and volume correlation for deformation and damage

characterisation of fibre-reinforced composites: A review, Composite Structures, vol. 315, 7 2023, p. 116994.
DOI: 10.1016/j.compstruct.2023.116994

[12] A. Zaplatić, Z. Tomičević, F. Hild, Characterization of woven composite material under multiaxial loading regimes using fe-based stereocorrelation, Acta Polytechnica CTU Proceedings, vol. 48, 2024, pp. 56–60.
DOI: 10.14311/APP.2024.48.0056

[13] A. Zaplatić, Z. Tomičević, X. Chang, P. Kosec, S. Roux, F. Hild, Advanced fe-based multimodal correlation analyses for the characterization of woven composite, Mechanical Systems and Signal Processing, vol. 224, 2024, p. 112079.
DOI: 10.1016/j.ymssp.2024.112079

[14] M. Mehdikhani, E. Steensels, A. Standaert, K. A. Vallons, L. Gorbatikh, S. V. Lomov, Multi-scale digital image correlation for detection and quantification of matrix cracks in carbon fiber composite laminates in the absence and presence of voids controlled by the cure cycle, Composites Part B: Engineering, vol. 154, 2018, pp. 138–147.
DOI: 10.1016/j.compositesb.2018.07.006

[15] A. Zaplatić, Z. Tomičević, D. Čakmak, F. Hild, Identifiability of ludwik's law parameters depending on the sample geometry via inverse identification procedure, Coupled Systems Mechanics, vol. 11, 2022, pp. 133–149.
DOI: 10.12989/csm.2022.11.2.133

[16] M. A. Sutton, F. Hild, Recent advances and perspectives in digital image correlation, Experimental Mechanics, vol. 55, 1 2015, pp. 1–8.
DOI: 10.1007/s11340-015-9991-6

[17] G. Besnard, F. Hild, S. Roux, "finite-element" displacement fields analysis from digital images: Application to portevin-le châtelier bands, Experimental Mechanics, vol. 46, 12 2006, pp. 789–803.
DOI: 10.1007/s11340-006-9824-8

[18] F. Hild, S. Roux, Comparison of local and global approaches to digital image correlation, Experimental Mechanics, vol. 52, 11 2012, pp. 1503–1519.
DOI: 10.1007/s11340-012-9603-7

[19] A. Vrgoč, Z. Tomičević, B. Smaniotto, F. Hild, Application of different imaging techniques for the characterization of damage in fiber reinforced polymer, Composites Part A: Applied Science and Manufacturing, vol. 150, 11 2021.
DOI: 10.1016/j.compositesa.2021.106576

[20] A. Chojnacka-Brożek, A. Liber-Kneć, S. Łagan, Compression behavior of dental flowable composites—digital image correlation and numerical analysis, Materials, vol. 17, 2024, no. 23.
DOI: 10.3390/ma17235853

[21] Z. Bergant, T. Kek, A. Maček, M. Halilovič, R. Šturm, Multiaxial characterization of cross-ply and quasi-isotropic flax biocomposites using a modified arcan fixture and digital image correlation, Polymer Testing, vol. 154, 2026, p. 109059.
DOI: 10.1016/j.polymertesting.2025.109059

[22] K. Chawla, S. I. Talabi, B. Rodriguez, V. Kumar, S. Kim, V. Kunc, A. A. Hassen, Benchmarking image processing techniques for porosity measurement in polymer additive manufacturing: Review and experimental analysis, Composites Part B: Engineering, vol. 307, 2025, p. 112857.
DOI: 10.1016/j.compositesb.2025.112857

[23] F. Hild, A. Bouterf, S. Roux, Measurement of kinematic fields via dic for impact engineering applications, International Journal of Impact Engineering, vol. 130, 2019, pp. 163–171.
DOI: 10.1016/j.ijimpeng.2019.04.007

[24] Y. Guo, M. Kabir, F. Mancini, P. J. Withers, J. H. S. Almeida, Microstructure-failure interactions in continuous carbon- and glass-fibre reinforced nylon 3d-printed composites under compression, Composites Science and Technology, vol. 285, 2026, p. 111788.
DOI: 10.1016/j.compscitech.2026.111788

[25] J. Ying, Y. Yang, D. Wu, W. Qiao, Q. Meng, Mechanical behavior and thermal stability of 3d-printed green mortar reinforced with recycled carbon fibers and fully recycled fine aggregates, Construction and Building Materials, vol. 541, 2026, p. 147813.
DOI: 10.1016/j.conbuildmat.2026.147813

[26] ASTM International, Standard Test Method for Compressive Properties of Rigid Plastics, ASTM D695-15, West Conshohocken, PA, 2015, designation: D695 – 15.

[27] J. Schindelin, I. Arganda-Carreras, E. Frise, Fiji: an open-source platform for biological-image analysis, Nat Methods, vol. 9, 2012, p. 676–682.
DOI: https://doi.org/10.1038/nmeth.2019

[28] N. Otsu, A threshold selection method from gray-level histograms, IEEE Transactions on Systems, Man, and Cybernetics, vol. 9, 1979, no. 1, pp. 62–66.

[29] H. Leclerc, J. Neggers, F. Mathieu, S. Roux, F. Hild, Correli 3.0, Patent, 2015, IDDN.FR.001.520008.000.S.P.2015.000.31500.

[30] Z. Tomičević, F. Hild, S. Roux, Mechanics-aided digital image correlation, The Journal of Strain Analysis for Engineering Design, vol. 48, 2013, no. 5, pp. 330–343.
DOI: 10.1177/0309324713482457

[31] A. Mendoza, J. Neggers, F. Hild, S. Roux, Complete mechanical regularization applied to digital image and volume correlation, Computer Methods in Applied Mechanics and Engineering, vol. 355, 2019, pp. 27–43.
https://hal.science/hal-02148780v1.
DOI: 10.1016/j.cma.2019.06.005

[32] A. Zaplatić, X. Chang, Z. Tomičević, S. Roux, F. Hild, Failure mechanism identification for multiaxially loaded woven composites using hybrid infrared-visible light correlation, Engineering Failure Analysis, vol. 192, 2026, p. 110787.
DOI: 10.1016/j.engfailanal.2026.110787